8-2014

A Statistical Study of Magnetic Field Fluctuations in the Dayside Magnetosheath and Their Dependence on Upstream Solar Wind Conditions

A. P. Dimmock
Aalto University

K. Nykyri
Embry-Riddle Aeronautical University, nykyrik@erau.edu

T. I. Pulkkinen
Aalto University

Scholarly Commons Citation

Dimmock, A. P., K. Nykyri, and T. I. Pulkkinen (2014), A statistical study of magnetic field fluctuations in the dayside magnetosheath and their dependence on upstream solar wind conditions, J. Geophys. Res. Space Physics, 119, 6231–6248, doi:10.1002/2014JA020009

AGU PUBLICATIONS

JGR

Journal of Geophysical Research: Space Physics

RESEARCH ARTICLE

10.1002/2014JA020009

Key Points:
- Magnetic fluctuations are visibly enhanced on the magnetosheath dawn flank
- Magnetosheath magnetic fluctuations are larger for southward IMF at magnetopause
- Magnetosheath magnetic fluctuations are larger for faster solar wind speeds

Correspondence to:
A. P. Dimmock,
andrew.dimmock@aalto.fi

Citation:
Dimmock, A. P., K. Nykyri, and T. I. Pulkkinen (2014), A statistical study of magnetic field fluctuations in the dayside magnetosheath and their dependence on upstream solar wind conditions, *J. Geophys. Res. Space Physics*, *119*, 6231–6248, doi:10.1002/2014JA020009.

Received 21 MAR 2014
Accepted 10 JUL 2014
Accepted article online 15 JUL 2014
Published online 11 AUG 2014

A statistical study of magnetic field fluctuations in the dayside magnetosheath and their dependence on upstream solar wind conditions

A. P. Dimmock[1,2], K. Nykyri[1,2], and T. I. Pulkkinen[1]

[1]School of Electrical Engineering, Aalto University, Espoo, Finland, [2]Department of Physical Sciences, Embry-Riddle Aeronautical University, Daytona Beach, Florida, USA

Abstract The magnetosheath functions as a natural interface connecting the interplanetary and magnetospheric plasma. Since the magnetosheath houses the shocked solar wind, it is populated with abundant magnetic field turbulence which are generated both locally and externally. Although the steady state magnetosheath is to date relatively well understood, the same cannot be said of transient magnetic perturbations due to their kinetic nature and often complex and numerous generation mechanisms. The current manuscript presents a statistical study of magnetic field fluctuations in the dayside magnetosheath as a function of upstream solar wind conditions. We concentrate on the ambient higher-frequency fluctuations in the range of 0.1 Hz → 2 Hz. We show evidence that the dawn (quasi-parallel) flank is visibly prone to higher-amplitude magnetic perturbations compared to the dusk (quasi-perpendicular) region. Our statistical data also suggest that the magnitude of turbulence can be visibly enhanced close to the magnetopause during periods of southward interplanetary magnetic field orientations. Faster (> 400 km s^{-1}) solar wind velocities also appear to drive higher-amplitude perturbations compared to slower speeds. The spatial distribution also suggests some dependence on the magnetic pileup region at the subsolar magnetopause.

1. Introduction

The magnetosheath (MS) is a region which functions as a natural interface between the solar wind (SW) and the magnetospheric plasma. At the point where the SW encounters the terrestrial magnetosphere (MSP), the supersonic solar wind velocities are rapidly reduced to subsonic values consequently forming a standing fast mode shock wave (BS) upstream of the planet. During this process, the SW kinetic energy is redistributed into other degrees of freedom and a small component of the particles are thermalized and accelerated to very high energies [*Sagdeev*, 1966; *Sagdeev and Galeev*, 1969; *Papadopoulos*, 1985]. The now "shocked" solar wind plasma occupies the magnetosheath and is hotter, denser, slower, and generally prone to a higher level of magnetic field turbulence compared to its upstream counterpart.

The plasma properties in the MS have received deserved attention since the early days of space plasma research in the form of theoretical, simulated, and experimental studies. For example, the early gas dynamic model by *Spreiter et al.* [1966] put in place the groundwork for understanding the spatial distribution of MS plasma properties. Additional simulated studies such as those based on magnetohydrodynamics (MHDs) [e.g., *Lyon*, 1994] have followed to further enhance our knowledge in the global behavior of MS plasma properties. Although MHD investigations offer improved flexibility over experimental-based studies, they are unable to resolve structures on the kinetic scale lengths. Alternative simulations such as particle-in-cell and hybrid codes go to some lengths to overcome these problems but are also not without their limitations. As a result of this, experimental studies [see *Petrinec et al.*, 1997; *Němeček et al.*, 2000; *Paularena et al.*, 2001; *Longmore et al.*, 2005; *Verigin et al.*, 2006; *Walsh et al.*, 2012; *Lavraud et al.*, 2013; *Dimmock and Nykyri*, 2013] are a necessity; however, the intricate processing of such data sets are not trivial.

Recent statistical studies performed by *Paularena et al.* [2001], *Longmore et al.* [2005], and *Walsh et al.* [2012] have shown very strong evidence of dawn dusk asymmetries of density, velocity, magnetic field strength, and ion temperature in the MS. *Paularena et al.* [2001] proposed a solar cycle dependence on the dawn-favored density asymmetry which could explain why *Dimmock and Nykyri* [2013] observed little to no clear ion density asymmetry between 2007 and 2013 since their data set includes data from both solar

cycles. It is still unclear what the specific driving mechanisms of these asymmetries are and whether there are strong dependencies on upstream conditions. On account of the accumulative research devoted to MS plasma properties, the steady state MS profile for parameters such as velocity, magnetic field, and density are relatively well understood and agree well with global MHD models [e.g., *Dimmock and Nykyri*, 2013]. On the contrary, the same statement does not apply to more transient features such as magnetic field and plasma velocity perturbations which may also play a key role in generating dawn/dusk asymmetries and the driving of various processes in the MS. In addition, such perturbations can directly affect properties such as electron and ion temperatures which are more sensitive to the kinetic rather than MHD physics.

The background MS magnetic field originates from the "frozen in" magnetic field in the SW plasma. This is transmitted across the BS and undergoes a compression and rotation needed for the conservation of the component normal to the shock surface. Inside the MS, the magnetic field lines are draped around the MSP which results in a MS magnetic field typically tangential to the MP [*Fairfield*, 1976]. The magnetic field strength is greatest around the subsolar region and appears to pile up around the stagnation point. The field strength then decreases tailward, and a stronger magnetic field typically remains behind the quasi-perpendicular shock resulting from the higher compression. Although this is generally an accurate description of the steady state magnetic profile and can be shown both experimentally [see *Dimmock and Nykyri*, 2013] and theoretically, it is only part of the complete picture. The MS is populated by abundant magnetic fluctuations and small-scale perturbations originating from various sources such as electromagnetic waves and instabilities. It still remains unclear what are the source of these fluctuations, how do we classify them, and what impact do they have on the global MS plasma properties. It is also important to investigate three possibilities: (1) are these fluctuations generated locally in the MS, (2) are they induced by magnetopause processes, or (3) are they generated upstream in the SW and then transmitted through the BS. The more likely scenario is that it is, in fact, a combination of the three.

Fairfield and Ness [1970] studied the magnetic field fluctuations in the magnetosheath by computing the power spectra (below 0.2 Hz) in a field-aligned coordinate system to distinguish between parallel and perpendicular fluctuations. They observed that compressional fluctuations were larger than the transverse fluctuations for lower frequencies, and the opposite was true at higher frequencies. It is also reported that the dawn MS exhibits a higher level of fluctuations compared to the dusk flank.

Fairfield [1976] reviewed the early literature on magnetic fields in the MS. For time-varying fields the author summarized that indeed there are multiple sources of waves contributing to the magnetic fluctuations typically observed in the MS. These waves originated from upstream waves convected across the BS, waves generated at the MP and BS, and waves generated locally in the MS by processes such as instabilities. It was also discussed that fluctuations tend to be gathered below the proton gyrofrequency.

Luhmann et al. [1986] investigated the spatial distribution of magnetic field fluctuations in the dayside MS. Their results showed convincing evidence that the quasi-parallel BS ($\Theta_{bn} < 45°$) is a predominant source of dayside MS magnetic fluctuations. They also proposed that as a direct result of this, the magnetic fluctuations in the dayside MS might be affected by the interplanetary magnetic field (IMF) orientation.

Mirror mode fluctuations have also been reported as a source of magnetic field fluctuations in the magnetosheath [see *Soucek et al.*, 2008; *Balikhin et al.*, 2010; *Soucek and Escoubet*, 2011]. An investigation into mirror mode fluctuations based on four-point Cluster data was performed by *Lucek et al.* [2001]. The authors analyzed two periods of mirror mode activity and reported that the scale of the mirror structures was least along the direction of the MP normal. Along the maximum variance direction, variations between spacecraft were observed at approximately 750 km.

Zastenker et al. [2002] used Interball-1/MAGION-4 and Interball-1/Geotail/IMP 8 spacecraft pairings to investigate magnetic field variations in the MS. The conclusions from their study was that magnetic field variations which range from seconds up to an hour are markedly larger than those observed simultaneously in the SW.

Shevyrev et al. [2007] performed a statistical study of low-frequency variations in the SW, foreshock, and MS using Interball-1 and Cluster measurements. They concluded that small-scale fluctuations in the MS were noticeably greater behind the quasi-parallel BS and, in general, the level of fluctuations increases as Θ_{bn} decreases.

Gutynska et al. [2008] studied the correlation lengths of MS fluctuations based on Cluster data. Their results suggested that the correlation length of the magnetic field fluctuations in the MS was approximately 1 Earth radii (R_E) and interestingly this only depended weakly on the ambient magnetic field direction. They also concluded that the response of magnetosheath properties were generally well predicted by the *Spreiter et al.* [1966] model.

Yao et al. [2011] performed a statistical study of electromagnetic field fluctuations in a finite region close to the MP. The authors calculated the energy spectral density of electromagnetic fluctuations with scales around the ion gyroradii. They reported that the energy spectral density was stronger across the MP and did not depend on the MS B_z component. They report that these fluctuations may facilitate additional plasma transport across the MP [*Johnson and Cheng*, 1997].

Gutynska et al. [2012] studied the relationship between MS magnetic field fluctuations and the foreshock. The authors concluded that fluctuations between frequencies of 10^{-4} and 10^{-2} Hz were observed in the MS except in close proximity to the MP. They also suggested that the amplitude of these fluctuations increased with decreased proximity to the MP, suggesting the MP as a significant driving mechanism.

Guicking et al. [2012] used Time History of Events and Macroscale Interactions (THEMIS) data to study wave activity in the Earth's MS for frequencies between 30 and 167 mHz. The authors reported that instabilities and other mechanisms driving electromagnetic waves in the MS are more likely to occur within close vicinity to the BS rather than deeper in the MS. They also suggested that the spatial distribution of wave activity in the MS could be related to the flow pattern of plasma around the MSP.

Recently, *Nykyri* [2013] presented evidence based on local MHD simulations that growth rates of Kelvin Helmholtz Instability (KHI) are significantly greater on the dawn MS flank (compared to dusk) during Parker-spiral (PS) IMF conditions. Such a result could explain the presence of fluctuations close to the MP and could also shed some light on recent reports of dawn-favored temperature asymmetries in the plasma sheet [*Wing et al.*, 2005].

The current manuscript builds on existing studies of MS magnetic field perturbations by applying our statistical mapping tool [see *Dimmock and Nykyri*, 2013] to quantify the amplitude and spatial distribution of magnetic field fluctuations in the dayside MS. Statistical maps of perpendicular and parallel magnetic field fluctuations between 0.1 and 2 Hz are presented for different upstream SW conditions to investigate the SW dependence. The manuscript is structured as follows. Section 2 outlines the details of the instrumentation and data sets that were used to complete this study. Section 3 discusses the methodology adopted to extract and quantify the magnetic field fluctuations from the time series data. Section 4 presents statistical maps of the magnetic field fluctuation amplitude for various upstream conditions. Section 5 discusses these results before drawing our conclusions in section 6.

2. Data Sets

The entirety of our MS statistical data originates from the array of instrumentation on board each of the five THEMIS spacecraft [*Angelopoulos*, 2008]. The present study utilizes THEMIS magnetic field and plasma measurements which span a time interval from October 2007 to October 2013. In situ magnetic field measurements are provided by the fluxgate magnetometers (FGMs) fitted to each probe [*Auster et al.*, 2008]. The FGM supplies full three-axis magnetic field measurements at a maximum revolution of 64 vector/s and a capacity for detecting perturbations of 0.01 nT. Since the availability of each data set differs, we use 4 Hz FGM resolution since it both provides the adequate sampling time and the coverage required to compile our statistical database. Other plasma properties such as velocity, density, and pressure are calculated on board by the electrostatic analyzer instrument [*McFadden et al.*, 2008].

In addition to MS measurements, we also require SW observations for prefiltering of statistical data and the evaluation of MP and BS models. These data are acquired from the OMNI database (http://omniweb.gsfc.nasa.gov), which provides upstream plasma properties at the BS nose [*King and Papitashvili*, 2005]. These observations are recorded at various upstream locations from several sources which are then propagated to the BS nose using the model by *Farris and Russell* [1994]. We use the highest resolution available which are the monthly 1 min resolution data files corresponding to the interval of available THEMIS data.

3. Methodology

The methodology adopted for this study will be discussed as two components. First is the transformation of THEMIS locations into the normalized MS system and the subsequent binning of these data. Second are the extraction and quantification of magnetic field fluctuations from the measured 4 Hz FGM time series data.

3.1. Transformation to the Model Magnetosheath

We transform each THEMIS data point initially in the GSE frame to the magnetosheath interplanetary medium (MIPM) reference frame. The reason for implementing this conversion is to (1) adjust for planetary aberration, (2) organize data points with respect to the shock geometry, and most crucially (3) to account for motion of the MS boundaries. The first point is addressed by aligning the *x* axis to the upstream SW flow vector and subtracting the orbital velocity (V_e) from the *y* component of the SW flow velocity vector.

$$\vec{\mathbf{e}}_{\mathbf{x}} = \frac{\left[-V_x, -V_y - V_e, -V_z\right]}{\sqrt{{V_x}^2 + (V_y + V_e)^2 + {V_z}^2}} \tag{1}$$

Please note that since the OMNI data are already corrected for planetary aberration, then removing the orbital velocity in the above equation is not required but mentioned for completeness. The adopted approach of (2) is to compute the *y* axis as a function of the upstream IMF vector.

$$\vec{\mathbf{e}}_{\mathbf{y}} = \begin{cases} -\vec{\mathbf{B}} + (\vec{\mathbf{B}} \cdot \vec{\mathbf{e}}_{\mathbf{x}})\vec{\mathbf{e}}_{\mathbf{x}} / |\vec{\mathbf{B}} - (\vec{\mathbf{B}} \cdot \vec{\mathbf{e}}_{\mathbf{x}})\vec{\mathbf{e}}_{\mathbf{x}}|, \text{ if } (\vec{\mathbf{B}} \cdot \vec{\mathbf{e}}_{\mathbf{x}}) > 0, \\ +\vec{\mathbf{B}} - (\vec{\mathbf{B}} \cdot \vec{\mathbf{e}}_{\mathbf{x}})\vec{\mathbf{e}}_{\mathbf{x}} / |\vec{\mathbf{B}} - (\vec{\mathbf{B}} \cdot \vec{\mathbf{e}}_{\mathbf{x}})\vec{\mathbf{e}}_{\mathbf{x}}|, \text{ if } (\vec{\mathbf{B}} \cdot \vec{\mathbf{e}}_{\mathbf{x}}) < 0 \end{cases} \tag{2}$$

The outcome will force the dawn and dusk flanks of the MS to correspond to plasma processed by a quasi-parallel and a quasi-perpendicular bow shock, respectively. This configuration most closely resembles an IMF vector aligned with a Parker-spiral orientation. To complete the three-axes set, the *z* axis is obtained by evaluating the cross product between $\vec{\mathbf{e}}_{\mathbf{x}}$ and $\vec{\mathbf{e}}_{\mathbf{y}}$:

$$\vec{\mathbf{e}}_{\mathbf{z}} = \vec{\mathbf{e}}_{\mathbf{x}} \times \vec{\mathbf{e}}_{\mathbf{y}} \tag{3}$$

The above axes are known as the geocentric interplanetary medium reference frame. To finalize the conversion to the MIPM frame, the zenith $\theta = \arccos((\mathbf{R} \cdot \mathbf{e}_{\mathbf{x}})/|\mathbf{R}|)$ and clock $\phi = \arctan((\mathbf{R} \cdot \mathbf{e}_{\mathbf{z}})/(\mathbf{R} \cdot \mathbf{e}_{\mathbf{y}}))$ angles are computed. Finally, these coordinates are then normalized between the *Shue et al.* [1998] MP and *Verigin et al.* [2001] BS model boundaries to provide a fractional distance across the MS:

$$F_{\text{mipm}} = \frac{|\vec{\mathbf{R}}| - r_{\text{MP}}(\theta)}{r_{\text{BS}}(\theta, \phi) - r_{\text{MP}}(\theta)} \tag{4}$$

In equation (4), r_{MP} and r_{BS} are the geocentric distances to the model MP and BS, respectively. The values of F_{mipm} in the MS range from 0 (MP) to 1 (BS). Everything across this range describes the normalized MS location between the boundaries. The above procedure is used to determine which region of space the THEMIS probes occupy at any given time. The value of F_{mipm} is used to compile a large statistical database of MS measurements which is then binned onto the MIPM *x-y* plane using a fixed square grid space with individual dimensions of $0.5 \times 0.5\ R_E$. The value assigned to each bin corresponds to the mean of plasma parameters whose *xy* MIPM location falls into each bin. These binned data sets are reproduced for different upstream SW conditions based on a 20 min average of the OMNI data. To ensure accurate determination of the SW conditions, we remove data where the SW cone angle variation exceeds 30° within each 20 min OMNI data interval. We removed these intervals since they introduce additional noise into the statistical maps due to transient changes in the BS geometry. After systematically studying the impact from the threshold of the cone angle variation, we selected a 30° limit as it provided the optimal balance between data coverage and statistical noise. To remove outliers resulting from inaccurate determination of the boundaries, we also impose a limitation that the MS flow speed must be slower than that of the SW. Although MS flow velocities exceeding the SW have been previously observed, the occurrence of these should be statistically much less than slower values given our current data set is limited to the dayside MS. Regarding outliners on the MSP side, we do not attempt to eliminate these data since simultaneous MSP data are not available as is the case with the SW measurements. Please refer to the recent paper by *Dimmock and Nykyri* [2013] for a more

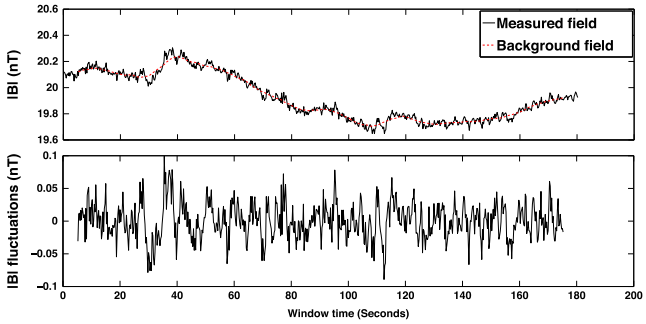

Figure 1. Demonstration of the extraction of magnetic field fluctuations from the measured 4 Hz THEMIS magnetic field data. (top) The measured (black) and background (red) magnetic fields. (bottom) The remaining magnetic field fluctuations.

detailed description of the binning process, further results, and direct comparisons with MHD simulations. We also refer the reader to *Verigin et al.* [2001, and references therein] for an additional thorough description of the models used and the MIPM frame.

3.2. Determination of Magnetic Field Fluctuations

Magnetic field turbulence in the MS is often associated with electromagnetic waves such as whistler, mirror mode, and kinetic Alfvén waves which are known to occupy the MS. Preferably, the physical process corresponding to the observations would be determined but spatial-temporal ambiguities make such investigations difficult especially on a statistical basis. This issue can be resolved using several techniques typically relying on theoretical models or techniques which are dependent on multispacecraft measurements [see *Hoppe et al.*, 1982; *Dimmock et al.*, 2013]. However, theoretical models can often be very specific which in turn provide limited applicability. Multiple spacecraft measurements on the other hand require the magnitude spacecraft separation vectors similar or less than the wave coherence scale and in very specific configurations. In addition to this, wave modes observed in the MS are dispersive by nature and influenced by Doppler shift. For that reason, large-scale statistical studies requiring the identification of specific wave modes are particularly difficult and can be prone to error due to the sensitivity of inaccurate assumptions such as the wave vector direction. Therefore, the present study focuses exclusively on the measured magnetic fluctuations in the spacecraft frame, and no attempt is made to identify the wave mode responsible.

Magnetic fluctuations are separated into components which are parallel ($B_{\parallel}$) and perpendicular ($B_{\perp}$) to the background magnetic field direction $\hat{\mathbf{b}}_0$. The direction of $\hat{\mathbf{b}}_0$ is determined from equation (5) below:

$$\hat{\mathbf{b}}_0 = \frac{\left[\overline{B}_x, \overline{B}_y, \overline{B}_z\right]}{\sqrt{\overline{B}_x{}^2 + \overline{B}_y{}^2 + \overline{B}_z{}^2}} \tag{5}$$

In equation (5) above, $\hat{\mathbf{b}}_0$ is evaluated over the 3 min window of the FGM 4 Hz THEMIS time series data. To extract the magnetic field fluctuations, the background DC field $\vec{\mathbf{B}}_{\mathrm{DC}}$ is estimated using a moving average filter (MAF) and then subtracted from the measured 4 Hz time series data. The duration of the MAF window (W) corresponds to a time interval of 10 s and is computed as follows:

$$\vec{\mathbf{B}}_{\mathrm{DC}}[i] = \frac{1}{W}\sum_{j=-W/2}^{W/2} B\left[i+j\right] \tag{6}$$

Following this, $\vec{\mathbf{B}}_{\mathrm{DC}}$ is removed from the measured magnetic field:

$$\vec{\mathbf{B}}_f = \vec{\mathbf{B}} - \vec{\mathbf{B}}_{\mathrm{DC}} \tag{7}$$

This process provides a "detrended" magnetic field which contain the magnetic fluctuations between 0.1 and 2 Hz parallel and perpendicular to $\hat{\mathbf{b}}_0$. Figure 1 shows an example of the process described by equations (6) and (7). Plotted in Figure 1 (top) are the measured magnetic field (black) and the DC trend (red) estimated from equation (6). Figure 1 (bottom) shows the detrended field described by equation (7). This process results in data loss per 3 min window equivalent to the length of the MAF. Therefore, the 3 min window is now reduced to approximately 2 min and 50 s. $\vec{\mathbf{B}}_f$ is now separated into parallel and perpendicular components where the parallel component is simply the projection of $\mathbf{B_f}$ along $\hat{\mathbf{b}}_0$:

$$B_{\parallel} = \mathbf{B_f} \cdot \hat{\mathbf{b}}_0 \tag{8}$$

Table 1. Preselection Criteria for Statistical Data Sets

Condition	Criteria
All conditions	n/a[a]
Northward IMF	$B_z > 0.5\|\vec{\mathbf{B}}\|$ nT
Southward IMF	$B_z < -0.5\|\vec{\mathbf{B}}\|$ nT
Slow SW	$\|\vec{\mathbf{V}}\| < 400$ km/s
Fast SW	$\|\vec{\mathbf{V}}\| > 400$ km/s

[a]No upstream selection applied.

and $B_\perp$ is calculated by subtracting $B_\parallel$ from $\vec{\mathbf{B}}_\mathbf{f}$:

$$B_\perp = \mathbf{B_f} - \hat{\mathbf{b}}_\mathbf{0} B_\parallel \tag{9}$$

We now compute the peak to peak of the magnitude of $B_\parallel$ and $B_\perp$ as shown in equation (10) below:

$$\begin{aligned} B_\parallel^{pk} &= \max|B_\parallel| - \min|B_\parallel| \\ B_\perp^{pk} &= \max|B_\perp| - \min|B_\perp| \end{aligned} \tag{10}$$

$B_\parallel^{pk}$ and $B_\perp^{pk}$ are computed using each 2 min 50 s THEMIS window and then subsequently binned in the same manner as the plasma parameters in *Dimmock and Nykyri* [2013].

4. Results

The preceding section presented methodology for the processing of the FGM 4 Hz time series data which are used to produce statistical maps of the magnetic field fluctuation amplitude in the dayside MS. We now present results of statistical data collected during northward IMF, southward IMF, fast SW, and slow SW in addition to the complete statistical database where no upstream filtering was performed. Each of these conditions can be found in the left-hand column of Table 1 together with the relevant selection criteria in the right-hand column. For each criteria listed in Table 1, we will present both the distribution of SW parameters and the statistical map of $B_\parallel^{pk}$ and $B_\perp^{pk}$.

4.1. Solar Wind Statistics

Presented in Figure 2 is a histogram of the SW parameters for the statistical data set absent of any upstream filtering. The IMF appears to be predominantly Parker-spiral as seen from the multiple "bumps" in the

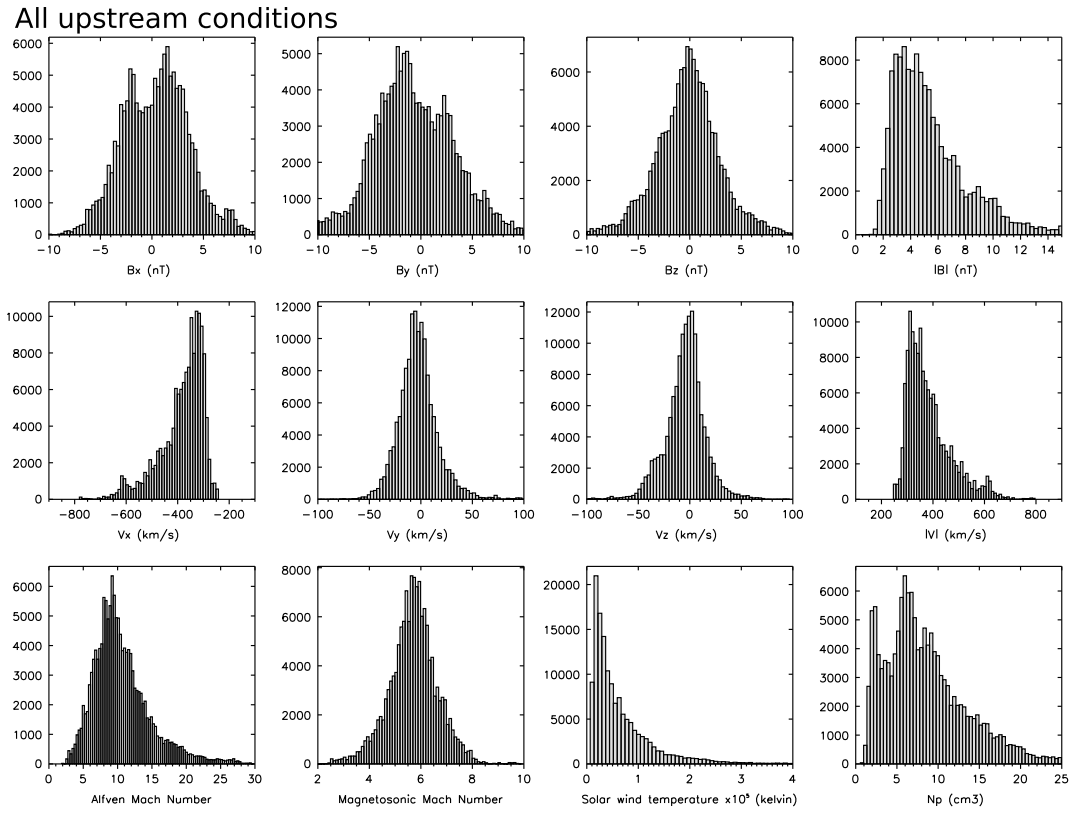

Figure 2. The above distributions show the solar wind statistics for data collected in the dayside magnetosheath during all upstream conditions.

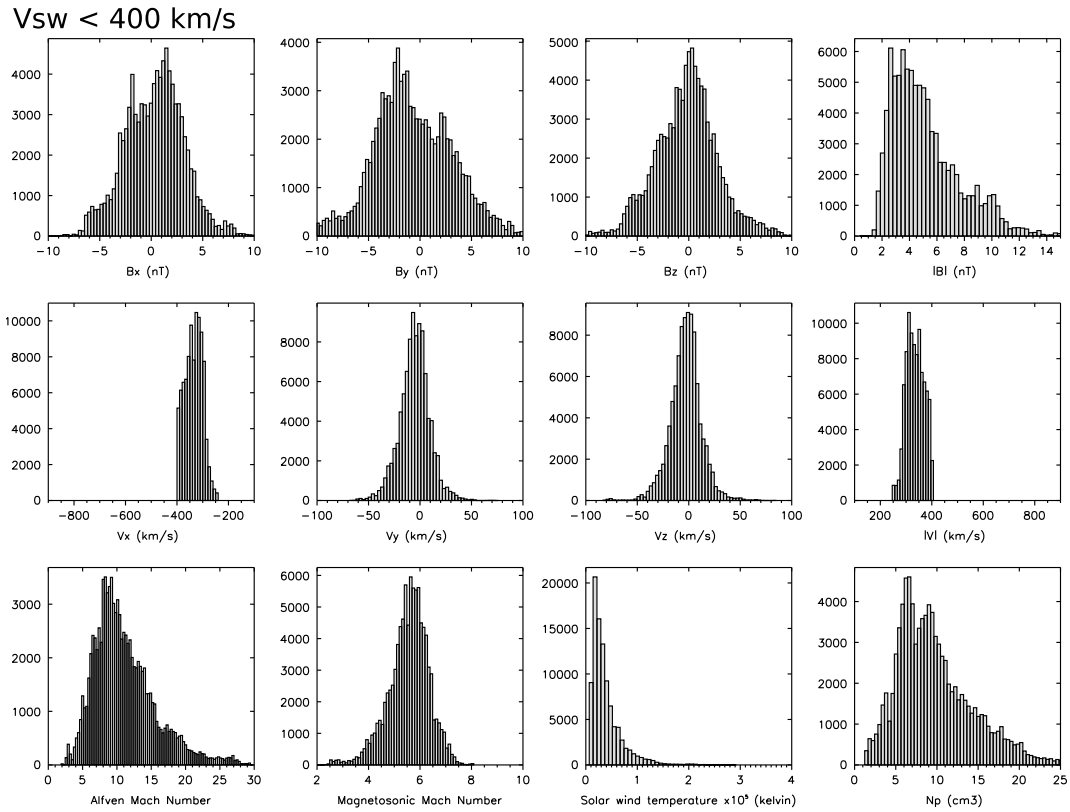

Figure 3. Solar wind statistics for data collected in the dayside magnetosheath when $|\mathbf{V}_{SW}| < 400$ km/s.

distributions of B_x and B_y suggesting inward and outward PS. The average magnitude of the SW velocity is around 400 km/s as indicated from the peak of the distribution of $|V_{sw}|$. The overall spread of SW velocities range from around 250 km/s up to 800 km/s which are common values of SW flow speeds. Note that the SW parameter distribution differs to those presented in *Dimmock and Nykyri* [2013] due to the difference in coverage of the 4 Hz FGM data, restriction of SW cone angle and the limitation to the dayside MS. The remaining distributions of SW parameters also suggest nothing atypical of expected SW parameters.

The histograms in Figures 3 and 4 illustrate the same plasma parameters as Figure 2 except that they are compiled for slow and fast SW, respectively. We refer you to Table 1 for details of how this is defined. Since the IMF is not taken into account in these databases, the Parker-spiral orientation remains evident from the similar bumps in B_x and B_y, though less apparent in Figure 4. There is a visible discrepancy between Figures 3 and 4, which are the changes in the distribution of ion temperature and ion number density. For the slow SW data set shown in Figure 3, the SW ion temperature is typically around 0.5×10^5 K and reaches maximum values of approximately 1.5×10^5 K. Direct comparison with the faster SW statistics suggests hotter plasma with a mean around 1.0×10^5 K extending to hotter temperatures around 4.0×10^5 K. There is a similar but inverse relationship when comparing ion number density. For the slow SW, typical values are centered around 7.5 per cm^3, whereas for faster SW speeds this is significantly less at approximately 2.5 per cm^3. In summary, faster SW flow is hotter but less dense compared to that of the slower SW. This is a characteristic of the fast and slow SW streams [*Bame et al.*, 1977; *Ebert et al.*, 2009] and could play a key role in dictating the properties of the MS.

Figures 5 and 6 show the distributions of the same SW parameters as the previous histogram plots but for northward and southward IMFs. The IMF orientation is clear from the distribution of the IMF B_z component. Other than this, there are very few differences between Figures 5 and 6. Comparison of Figures 5 and 6 with Figure 2 offered only one difference which is the absence of the Parker-spiral nature of the SW. Apart from this (expected) dissimilarity, the distribution on SW parameters appear to be centered around (and range from) very similar values to those in Figure 2. This particular comparison is important since any differences

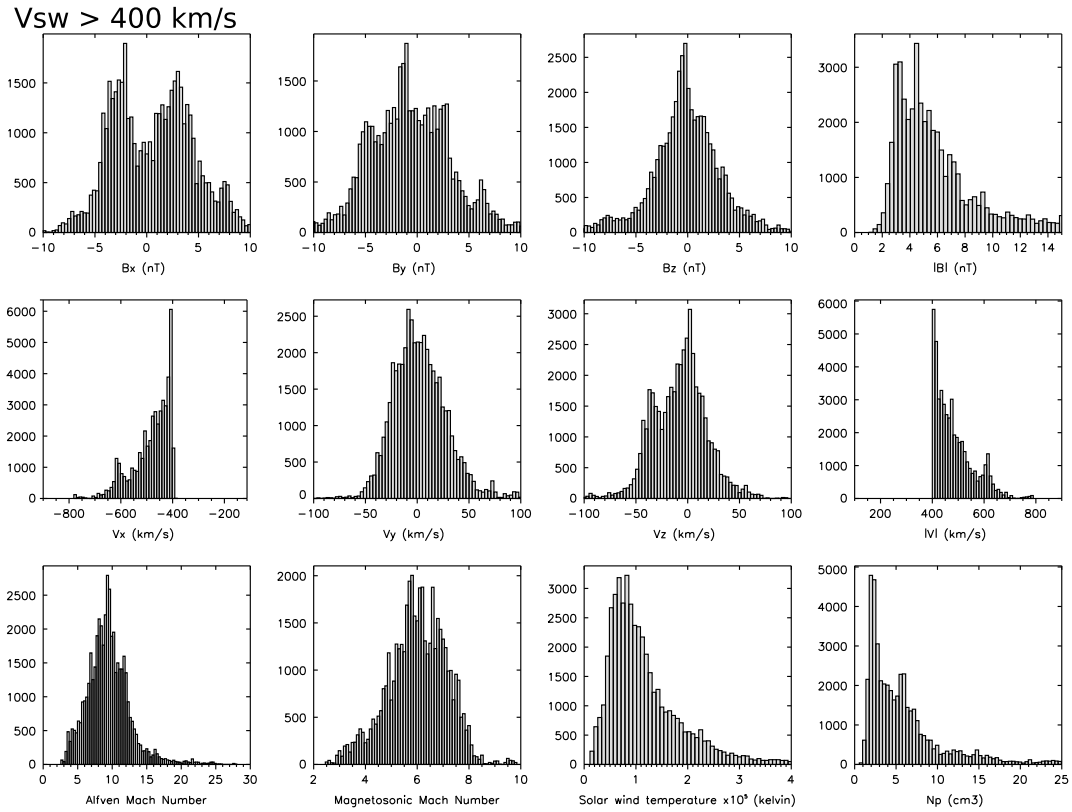

Figure 4. Solar wind statistics for data collected in the dayside magnetosheath when $|\mathbf{V}_{SW}| > 400$ km/s.

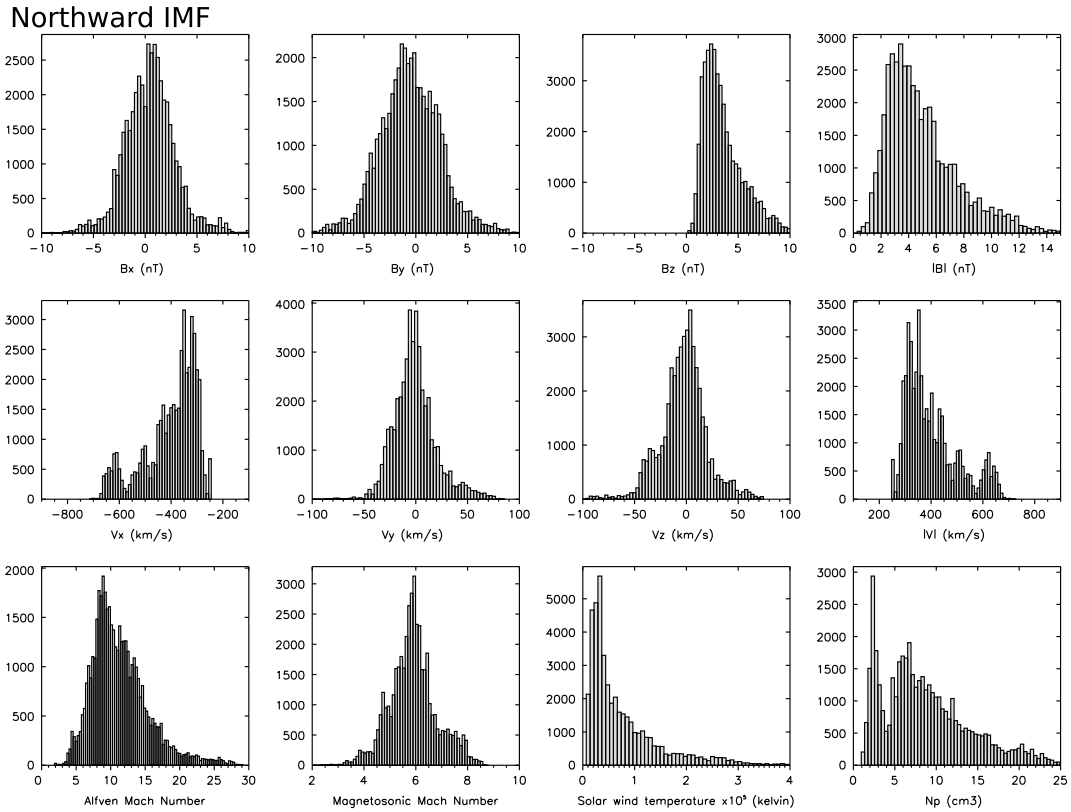

Figure 5. Solar wind statistics for data collected in the dayside magnetosheath during northward IMF conditions.

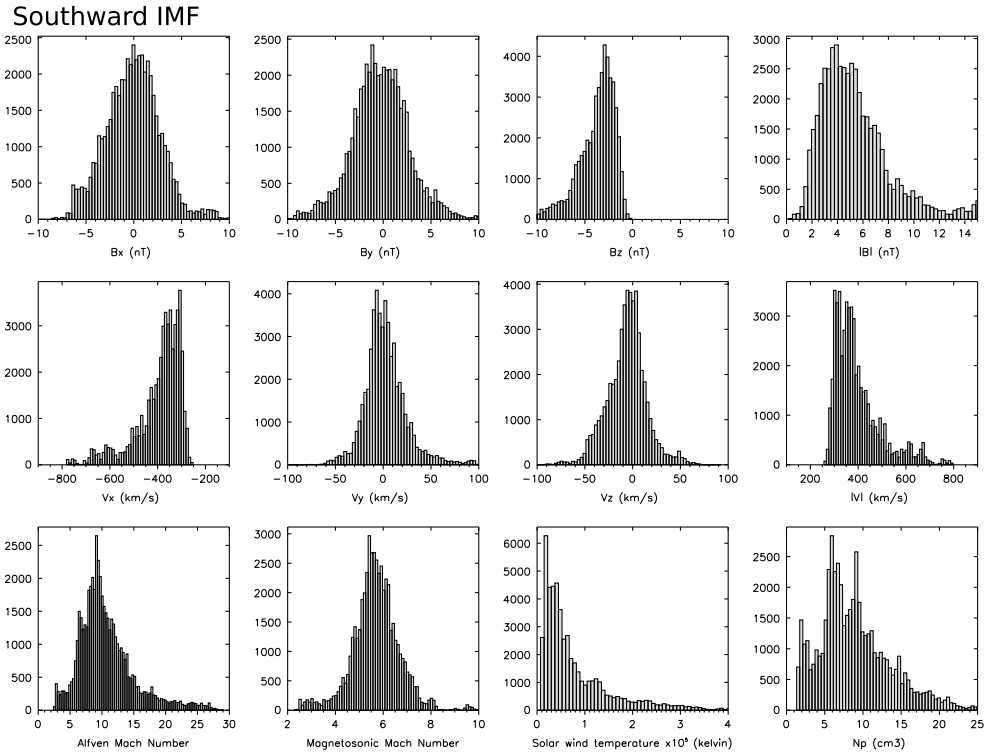

Figure 6. Solar wind statistics for data collected in the dayside magnetosheath during southward IMF conditions.

in the statistical maps based on the data in Figures 5 and 6 should be a consequence of the IMF orientation and no other SW parameters.

4.2. Statistical Maps for All Upstream Conditions

Presented in Figure 7 are the statistical maps of $B_{\parallel}^{pk}$ (Figure 7a) and $B_{\perp}^{pk}$ (Figure 7b) for the complete statistical data set corresponding to the SW statistics shown in Figure 2. The data coverage for this map is plotted

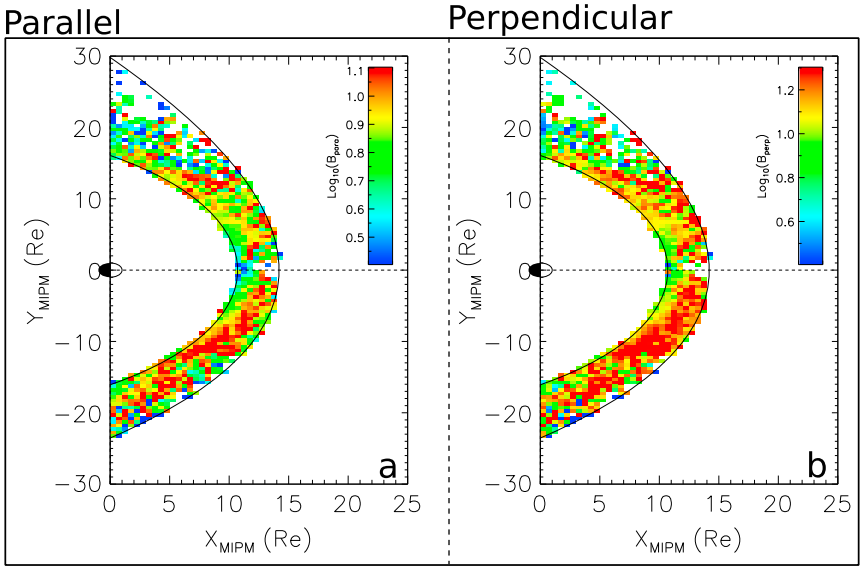

Figure 7. Statistical maps of (a) $B_{\parallel}$ and (b) $B_{\perp}$ binned for all upstream solar wind conditions.

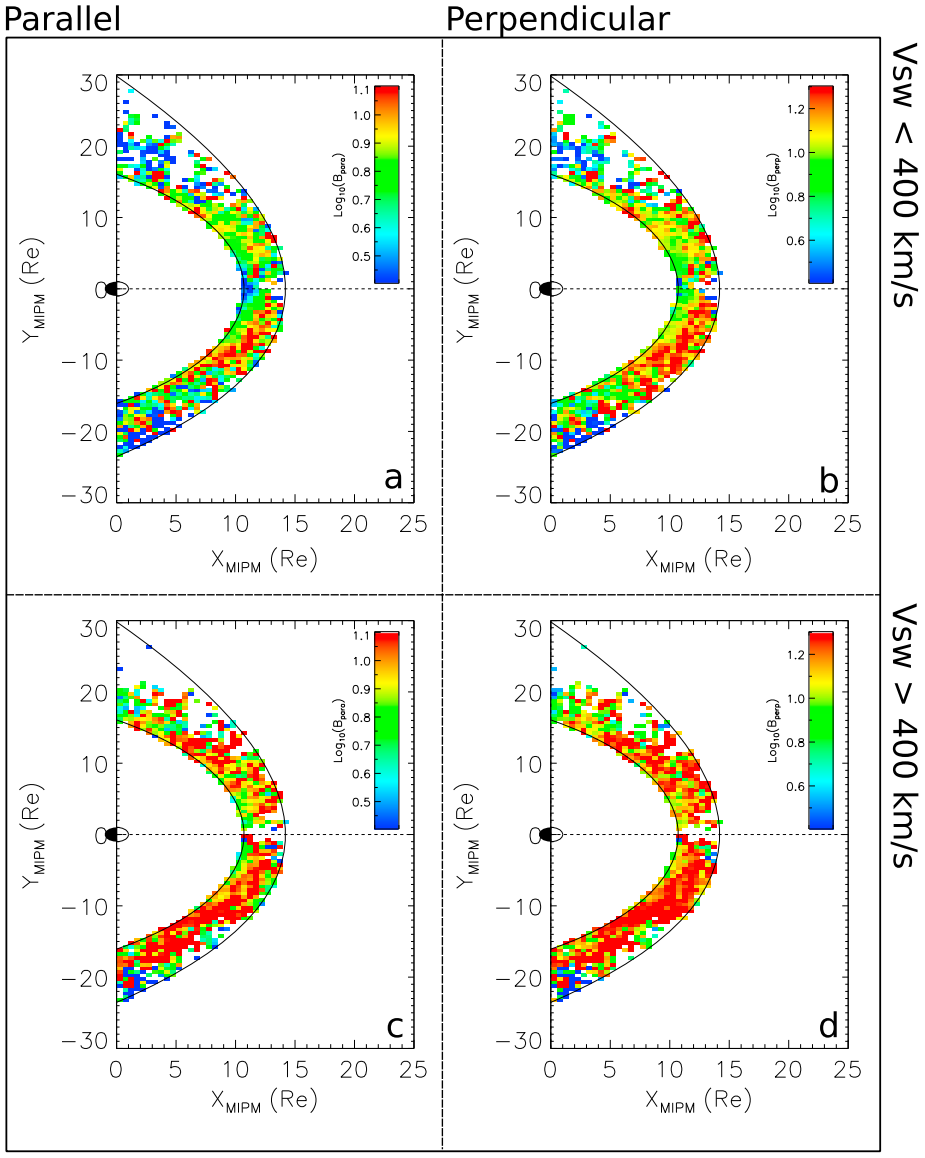

Figure 8. Statistical maps of (a, c) $B_{||}$ and (b, d) $B_{\perp}$ binned for $|\vec{V_{sw}}| < 400$ km/s shown in Figures 8a and 8b and $|\vec{V_{sw}}| > 400$ km/s shown in Figures 8c and 8d.

in Figure A2a located in Appendix A. It is worth mentioning that during each map there is poor coverage at local noon particular close to the BS. Data placed at local noon in the MIPM frame require very strong radial IMF when the spacecraft is at that location. The mentioned conditions are statistically rare, and therefore, the coverage is reduced in this region. We therefore avoid drawing strong conclusions based on regions showing poor bin densities. The typical bin density for the complete database is roughly 75 points per bin up to 3 h from noon and 50 thereafter. Please note that each point per bin corresponds to a 3 m THEMIS interval. There are regions of poor coverage particularly close to the dusk terminator, and thus, we will avoid making conclusions based on data collected at these locations. Direct comparison of panels a and b reveals that although the spatial distributions are quite similar, the values of $B_{\perp}^{pk}$ are, in general, greater than $B_{||}^{pk}$. Figure A4 (Appendix A) shows $B_{||}^{pk}$ and $B_{\perp}^{pk}$ plotted on the same color scale confirming $B_{\perp}^{pk} > B_{||}^{pk}$. Numerical cuts performed on each map estimate that the magnitude of $B_{\perp}^{pk}$ is typically 8–4 nT larger than $B_{||}^{pk}$. Evident in both panels are clear regions of enhanced magnetic fluctuations which are estimated (from the numerical data) on the dawn flank to be approximately 12 nT for $B_{||}^{pk}$ and 18 nT for $B_{\perp}^{pk}$. An interesting feature

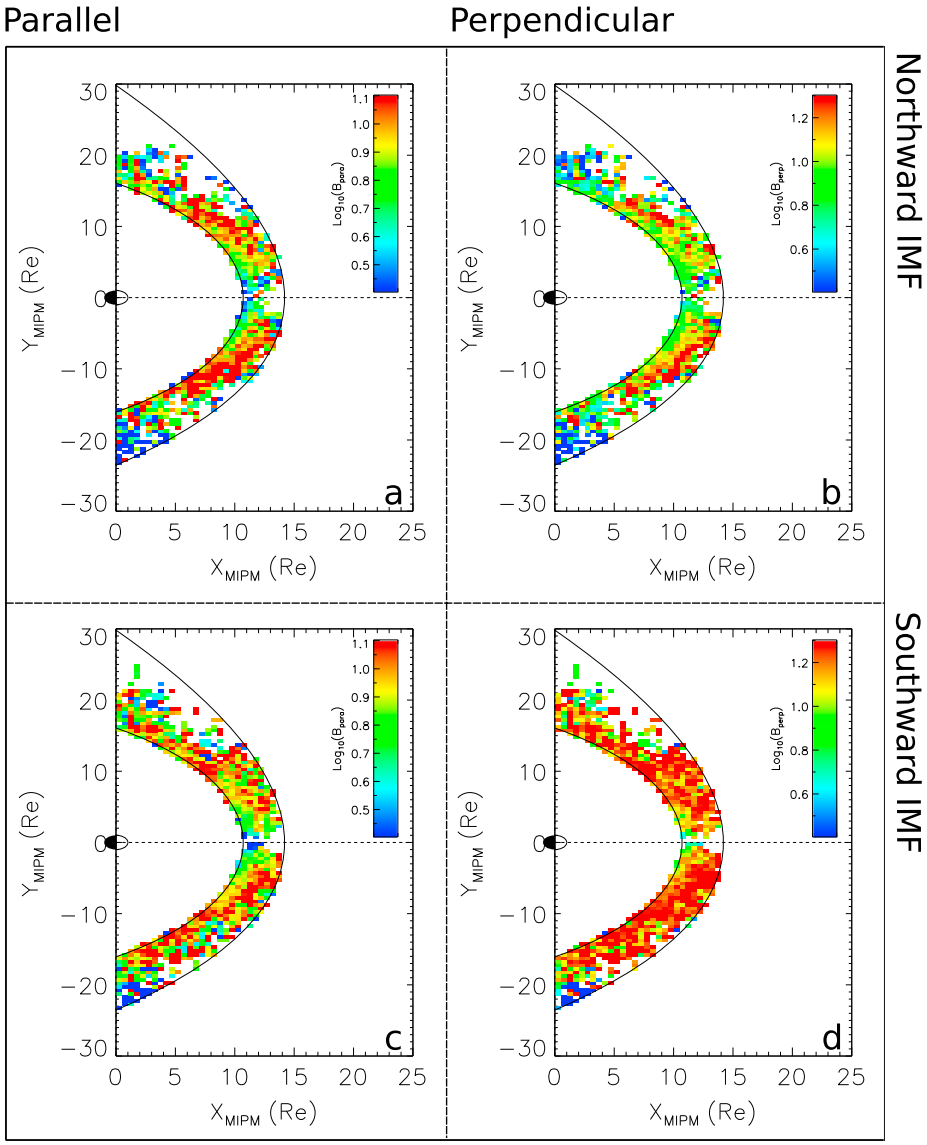

Figure 9. Statistical maps of (a, c) $B_{\parallel}$ and (b, d) $B_{\perp}$ binned for northward IMF shown in Figures 9a and 9b and southward IMF shown in Figures 9c and 9d.

in both panels is that on the dusk flank, the fluctuation amplitude is calculated to be reduced by roughly 20–25% suggesting a dawn-favored asymmetry. We produced maps of the standard error of the mean (SEM = $\sigma/\sqrt{n}$, where n is the bin number density and σ represents standard deviation) (see Figure A3 in Appendix A) for each bin which suggested limits of the mean to be typically 1 nT ranging to 1.5 nT in some isolated regions. The reported asymmetry is typically around 4–5 nT which is below the SEM. In both panels the spatial distribution of these enhanced regions are remarkably similar. At 0–2 h (close to the MP) from noon this region appears to be separated from the MP nose at a distance of 1–2 R_E. On the other hand, at roughly 3 h from noon this enhanced region extends to the MP. A logical observation is that the spatial distribution of this enhanced region is inversely correlated with that of magnetic field strength since it appears to correspond to the magnetic pileup region. The physical meaning of this will be discussed at greater detail in the following section.

4.3. Statistical Maps Based on Solar Wind Velocity

Figure 8 shows the statistical maps of the same quantities presented in Figure 7 binned separately for fast and slow solar wind velocities. Panels a and b represent the slow (< 400 km/s) SW (see Figure 3), whereas

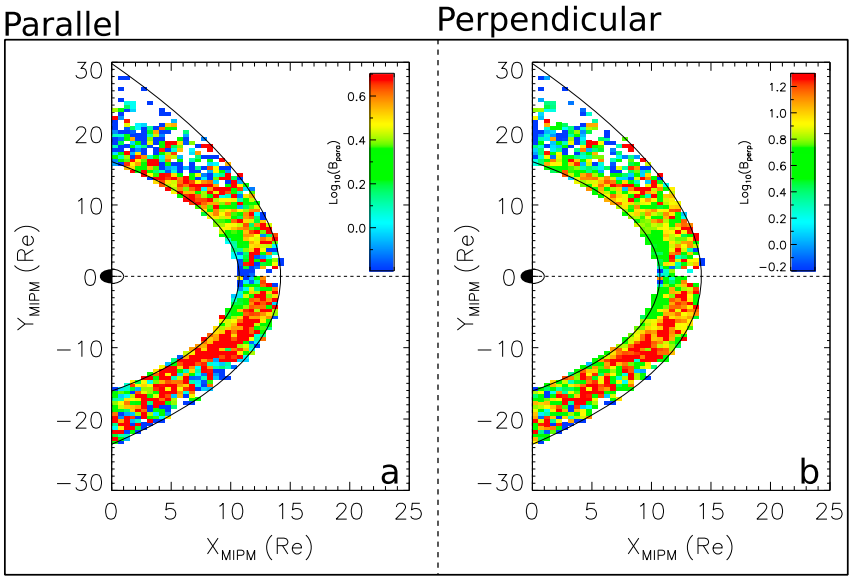

Figure 10. Statistical maps of the variance of $B_{||}$ and $B_{\perp}$ for all upstream conditions.

panels c and d correspond to the faster (> 400 km/s) SW data set (see Figure 4). According to Figure A2 the typical bin density for slow SW is estimated as 35 points per bin 0–3 h from noon and approximately 20 further toward the terminator. For the faster SW, the bin density is similar although coverage appears to be slightly reduced. Nevertheless, the dayside MS 0-4 h from noon offers ample coverage with typically an excess of 50 points per bin. Although comparing Figures 7 and 8 imply little difference in terms of the spatial distribution of the fluctuations, there is a notable discrepancy in the magnitude. During faster SW conditions the MS is populated with much higher-amplitude fluctuations than during slower SW velocities and typical conditions (see Figure 7). The dawn/dusk asymmetry remains for both statistical maps and does not appear to vary with respect to Figure 7.

4.4. Statistical Maps Based on Northward and Southward IMF Orientations

Figure 9 presents the statistical maps of $B_{||}^{pk}$ and $B_{\perp}^{pk}$ for data collected during northward (Figures 9a and 9b) and southward IMF (Figures 9c and 9d). Since the SW is statistically aligned with a Parker-spiral orientation then there are less data available during northward and southward IMFs. To compensate, we have removed the 30° limitation on the SW clock angle since we have reproduced the statistical data with this condition enforced and it had little to no impact on our results except reducing the data coverage. The average bin densities for northward and southward IMFs are estimated to be approximately 35 points per bin. The available coverage is limited beyond 4 h from noon; therefore, we will refrain from basing our interpretations from data binned outside of this region. There is an obvious difference between Figures 9b and 9d suggesting that the magnitude of $B_{\perp}^{pk}$ is larger during periods of southward IMF than northward IMF. The amplitude of $B_{\perp}^{pk}$ close to the MP have also increased over those measured during typical SW conditions. Interestingly, this does not seem to have the same impact on $B_{||}^{pk}$ in which there is very little change in the magnitude of the fluctuations. Similar to the results presented in Figure 8 the distance between the region of enhanced fluctuations and the MP around noon also varies which is anticorrelated to the spatial distribution of the magnetic field strength during these conditions (see Appendix A, Figure A1). Interestingly, during southward IMF, the dawn/dusk asymmetry appears to be reduced (shown in Figures 7 and 8) to a point where it is much weaker. We estimate this asymmetry to be around 5–10% corresponding to a numerical difference of around 2 nT. This is interesting since the previous statistical maps have been compiled for a statistical Parker-spiral IMF and the asymmetry was notably larger. Comparison of Figures 7 and 9 gives a strong indication that during periods of southward IMF, the amplitudes of the perpendicular fluctuations in the vicinity of the MP (i.e., $0 \leq F_{mipm} \leq 0.33$) are increased.

5. Discussion

In the current paper we have studied the spatial distribution of magnetic field fluctuations between 0.1 and 2 Hz in the dayside MS as a function of upstream SW conditions. Magnetic field perturbations were extracted from the FGM time series data and separated into components parallel and perpendicular to the background field direction (see equations (5) to (9)). Our previously developed statistical mapping tool [see *Dimmock and Nykyri*, 2013] was then used to create statistical maps of the peak to peak magnitude of the fluctuation amplitude ($B_{\parallel}^{pk}$ and $B_{\perp}^{pk}$) during periods of fast SW, slow SW, northward IMF, and southward IMF. We then visually compared these statistical maps with the same map produced for the complete data set representing "typical" conditions.

The first of our statistical data presented in Figure 7 were binned for all upstream SW conditions and reveal a noticeable dawn-favored asymmetry for the amplitude of magnetic field fluctuations in the dayside MS. With the exception of the IMF orientation, the distribution of SW parameters shown in Figure 2 suggests no individual parameter bias that could be responsible. The data coverage map shown in Figure A2 also suggests that there is adequate data coverage at these locations. We also compiled the statistical map for variance (shown in Figure 10) and arrive at the same result. Since the IMF orientation in these statistical data closely resemble a Parker-spiral orientation, our results agree with numerous studies [e.g., *Fairfield and Ness*, 1970; *Luhmann et al.*, 1986; *Zastenker et al.*, 2002; *Němeček et al.*, 2002; *Shevyrev and Zastenker*, 2005; *Shevyrev et al.*, 2006, 2007] reporting stronger magnetic field turbulence behind the quasi-parallel BS. Nevertheless, this is no surprise since it is well documented that downstream of quasi-parallel shocks, the plasma is more turbulent, or "perturbed," than their quasi-perpendicular counterparts [*Fairfield*, 1976]. It should also be mentioned that the foreshock plays a fundamental role in which backstreaming/reflected particles interact with the SW flow driving various upstream electromagnetic wave activity and instabilities [*Russell and Hoppe*, 1983]. Consequently, these electromagnetic waves and nonlinear magnetic structures are directed back toward the BS providing a source of MS turbulence [*Hoppe et al.*, 1981].

Data were also binned for fast and slow SW speeds and were presented in Figure 8. In these data, the dawn-favored asymmetry is still present but displayed a visible impact on the amplitude of the fluctuations. The asymmetry remained under different SW speeds suggesting that the SW speed does not primarily drive the asymmetry. This is also reasonable considering that the IMF orientation remains PS for the complete database, slow SW, and fast SW data sets. This is also supported by the lack of any strong asymmetry shown during northward and southward IMFs where the shock geometry is more symmetric. The amplitude on both dawn and dusk flanks are visibly enhanced during faster SW flow compared to intervals of slower speeds. This could be a result of the electromagnetic wave activity (such as mirror mode, ion cyclotron, and whistler waves) commonly observed in the vicinity of collisionless shocks [e.g., *Lacombe et al.*, 1995; *Schwartz et al.*, 1996; *Czaykowska et al.*, 2001; *Wilson et al.*, 2013] which are enhanced during intervals of higher SW velocities. During these periods, additional dissipation mechanisms [*Kennel et al.*, 1985; *Gosling et al.*, 1989; *Scholer and Terasawa*, 1990] are required which manifest as magnetic field turbulence/perturbations in the time series data. As a result of this, we attribute the increase in the amplitude of fluctuations in Figure 8 to the increased level of turbulence generated at (and immediately downstream of) the shock front. Regarding the dawn/dusk asymmetry; since the IMF orientation remains relatively unchanged from Figure 7 (Parker-spiral), the larger-amplitude fluctuations on the dawn flank should still be present.

Figure 9 shows the statistical maps for data collected when the IMF was strongly northward and southward based on the conditions outlined in Table 1. We refer to strong northward and southward IMFs since we require the B_z component to be greater and less than $0.5|\mathbf{B}|$ and $-0.5|\mathbf{B}|$, respectively. During southward IMF (Figure 9d), the amplitude of $B_{\perp}^{pk}$ is larger than those binned during all SW conditions shown in Figure 7b. The additional turbulence during a southward IMF could be explained by the existence of processes which favor a southward IMF orientation such as flux transfer events (FTEs) [*Russell and Elphic*, 1979] and subsolar reconnection [*Dungey*, 1961]. In addition, KHI can also operate during southward IMF [*Hwang et al.*, 2011], adding to the level of turbulence at the MP. For southward IMF, subsolar reconnection produces FTEs propagating tailward along the flank boundaries that typically cause bipolar variations

of the normal component of the magnetopause magnetic field [*Sibeck*, 1992]. The magnetic field lines surrounding the perturbed (either due to KHI or FTEs) magnetopause would also be perturbed, which will manifest as a turbulent signature in MS data set. The mutual interaction between the KHI and FTEs would likely produce a more turbulent magnetopause than when either mechanism would operate by themselves which could explain why the perpendicular turbulence is more enhanced for southward IMF at the MP (resulting from FTEs and the interaction of the FTEs and KHI). In addition, the increase in magnetic fluctuations for southward IMF (in the MS around the MP) is unlikely due to the error in the MP location and subsequent inclusion of magnetospheric data since this would most likely manifest as a reduction in magnetic field fluctuations. The decrease in the dawn/dusk asymmetry during northward and southward IMF intervals is likely to coincide with the approximate symmetry of the bow shock geometry on both flanks during these intervals. Although the estimated asymmetry is close to the SEM, our conclusion is not the magnitude of the asymmetry itself but the significant reduction compared to the other data sets during a PS IMF. Therefore, the effects discussed earlier in this section relating to the dawn-favored asymmetry (Figure 7) are not as effective when the IMF is strongly northward/southward. Close to the MP nose 0–2 h from noon (around the MP) there is a region of reduced amplitude perturbations which appears more prominent when the SW is strongly northward. These regions appear to inversely correspond to the magnetic pileup region which also increases in size during northward IMF conditions (see Figure A1). The enhanced magnetic field strength at the pileup region creates additional magnetic tension acting to restore the field, effectively impeding the development of perturbations. As already mentioned, the subsolar region possesses relatively low bin densities which should be noted. However, this feature also appears in areas further tailward which show higher densities and therefore is unlikely a manifestation of poor data coverage. Although interesting, the comprehensive investigation of this feature is beyond the scope of the current study and warrants a further, more rigorous study at a later date.

6. Conclusions

We have performed a statistical study of the amplitude of magnetic field fluctuations in the dayside magnetosheath using 6 years of THEMIS data. We have produced statistical maps for different solar wind conditions to study their relationship to upstream parameters. The main conclusions from our results are the following:

1. The amplitude of magnetic field fluctuations in the dayside magnetosheath are typically larger on the quasi-parallel (dawn) flank during a Parker-spiral interplanetary magnetic field (IMF) orientation.
2. The fluctuation amplitude appears to increase for periods of fast solar wind conditions (>400 km/s).
3. During intervals of southward IMF, there appears to be no significant dawn/dusk asymmetry.
4. The level of fluctuations close to the magnetopause increases during southward IMF.
5. The spatial distribution of magnetic perturbation amplitude implies a level of dependence on the profile of magnetic field strength particularly close to the subsolar magnetopause.

We conclude that upstream solar wind conditions have a significant impact on the amplitude of magnetic field perturbations in the magnetosheath particularly IMF orientation and solar wind velocity. Although identifying the exact source of magnetic field perturbations are difficult, we suspect that during typical solar wind conditions, (Parker-spiral) BS processes (and the foreshock) are the significant source of magnetosheath fluctuations; but during southward IMF, the processes at the magnetopause can drive higher-amplitude fluctuations at significant distance from the boundary. Although the present study goes to some lengths to understanding the solar wind driving of magnetosheath fluctuations, an investigation into the dependence of the spatial and temporal scales of the turbulence warrants further study.

Appendix A: Supplementary Statistical Maps

Figure A1 shows the statistical maps of the normalized (with respect to SW) magnetic field strength during intervals of northward (Figure A1, left) and southward (Figure A1, right) IMFs.

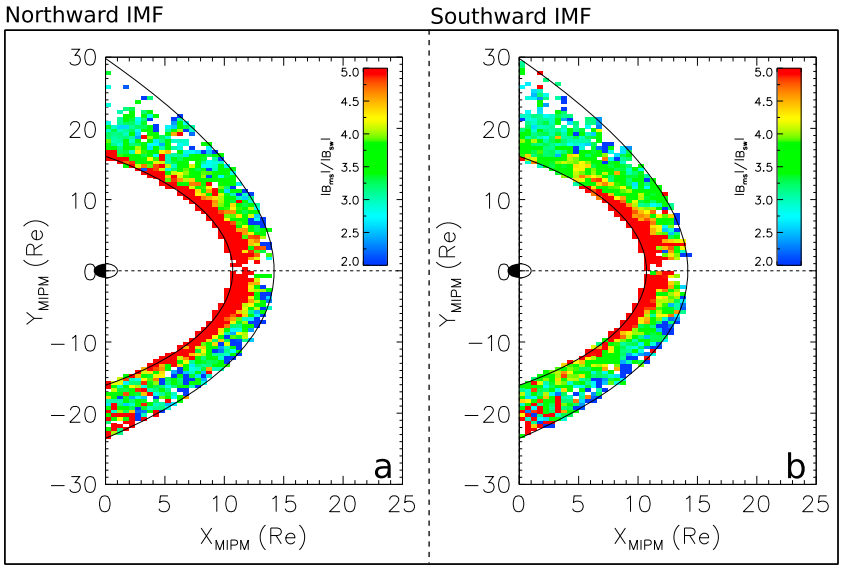

Figure A1. Normalized magnetic field strength binned for northward and southward IMF orientations.

Figure A2 presents the data coverage in terms of counts per bin for each statistical map produced in the main manuscript. The individual condition is labeled above each panel.

The statistical maps showing the variance of $B_{\parallel}^{pk}$ and $B_{\perp}^{pk}$ are plotted in Figure 10 which were computed as follows:

$$\sigma_{\parallel}{}^2 = \frac{1}{N}\sum_{i=1}^{n}\left(B_{\parallel} - \bar{B}_{\parallel}\right)^2$$
$$\sigma_{\perp}{}^2 = \frac{1}{N}\sum_{i=1}^{n}\left(B_{\perp} - \bar{B}_{\perp}\right)^2 \quad \text{(A1)}$$

The window length N corresponds to 2:50 min.

Figure A3 shows the statistical maps of the standard error of the mean, SEM = $\sigma/\sqrt{nb}$ for each bin reproduced for the complete database, slow SW, fast SW, northward IMF, and southward IMF.

Figure A4 shows $B_{\parallel}^{pk}$ (Figure A4a) and $B_{\perp}^{pk}$ (Figure A4b) plotted on the same color scale for comparison.

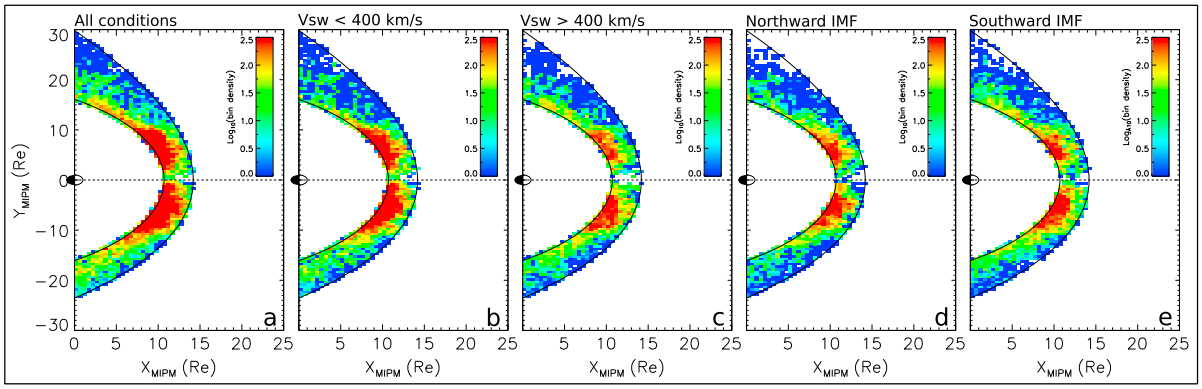

Figure A2. Statistical maps of data coverage plotted as bin number density for all conditions, slow SW, fast SW, northward IMF, and southward IMF.

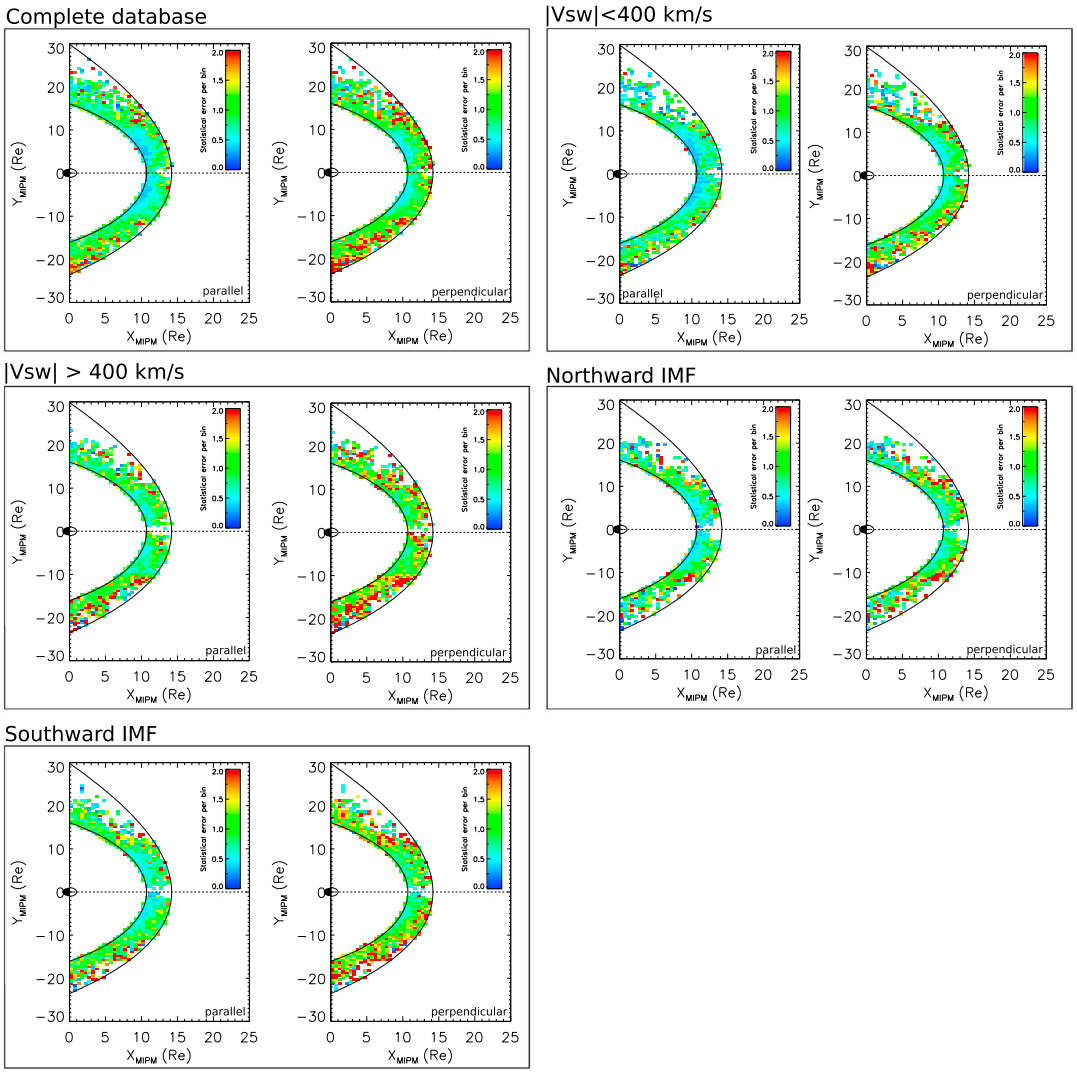

Figure A3. Statistical maps of the standard error of the mean for each bin replicated for the maps presented in the main manuscript.

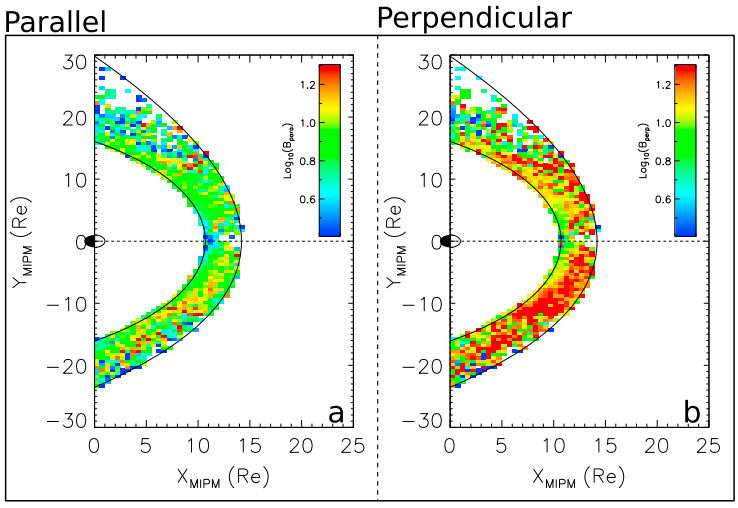

Figure A4. Statistical maps of (a) $B_{\parallel}$ and (b) $B_{\perp}$ binned for all upstream solar wind conditions mapped to the same color scale for comparative purposes.

Acknowledgments
The work by A. Dimmock and K. Nykyri was supported by the NSF grant 0847120 and the Academy of Finland grant 267073/2013. The OMNI data were obtained from the GSFC/SPDF OMNIWeb interface at http://omniweb.gsfc.nasa.gov. Authors would also like to thank the THEMIS instrument teams for providing the MS measurements required to complete this study.

Larry Kepko thanks Hui Zhang and another reviewer for their assistance in evaluating this paper.

References

Angelopoulos, V. (2008), The THEMIS mission, *Space Sci. Rev.*, *141*, 5–34, doi:10.1007/s11214-008-9336-1.
Auster, H. U., et al. (2008), The THEMIS fluxgate magnetometer, *Space Sci. Rev.*, *141*, 235–264, doi:10.1007/s11214-008-9365-9.
Balikhin, M. A., O. A. Pokhotelov, S. N. Walker, R. J. Boynton, and N. Beloff (2010), Mirror mode peaks: THEMIS observations versus theories, *Geophys. Res. Lett.*, *37*, L05104, doi:10.1029/2009GL042090.
Bame, S. J., J. R. Asbridge, W. C. Feldman, and J. T. Gosling (1977), Evidence for a structure-free state at high solar wind speeds, *J. Geophys. Res.*, *82*, 1487–1492, doi:10.1029/JA082i010p01487.
Czaykowska, A., T. M. Bauer, R. A. Treumann, and W. Baumjohann (2001), Magnetic field fluctuations across the Earth's bow shock, *Ann. Geophys.*, *19*(3), 275–287.
Dimmock, A. P., and K. Nykyri (2013), The statistical mapping of magnetosheath plasma properties based on THEMIS measurements in the magnetosheath interplanetary medium reference frame, *J. Geophys. Res. Space Physics*, *118*, 4963–4976, doi:10.1002/jgra.50465.
Dimmock, A. P., M. A. Balikhin, S. N. Walker, and S. A. Pope (2013), Dispersion of low frequency plasma waves upstream of the quasi-perpendicular terrestrial bow shock, *Ann. Geophys.*, *31*, 1387–1395, doi:10.5194/angeo-31-1387-2013.
Dungey, J. W. (1961), Interplanetary magnetic field and the auroral zones, *Phys. Rev. Lett.*, *6*, 47–48, doi:10.1103/PhysRevLett.6.47.
Ebert, R. W., D. J. McComas, H. A. Elliott, R. J. Forsyth, and J. T. Gosling (2009), Bulk properties of the slow and fast solar wind and interplanetary coronal mass ejections measured by Ulysses: Three polar orbits of observations, *J. Geophys. Res.*, *114*, A01109, doi:10.1029/2008JA013631.
Fairfield, D. H. (1976), Magnetic fields of the magnetosheath, *Rev. Geophys. Space Phys.*, *14*, 117–134, doi:10.1029/RG014i001p00117.
Fairfield, D. H., and N. F. Ness (1970), Magnetic field fluctuations in the Earth's magnetosheath, *J. Geophys. Res.*, *75*, 6050–6060, doi:10.1029/JA075i031p06050.
Farris, M. H., and C. T. Russell (1994), Determining the standoff distance of the bow shock: Mach number dependence and use of models, *J. Geophys. Res.*, *99*, 17,681–17,689, doi:10.1029/94JA01020.
Gosling, J. T., M. F. Thomsen, S. J. Bame, and C. T. Russell (1989), Ion reflection and downstream thermalization at the quasi-parallel bow shock, *J. Geophys. Res.*, *94*, 10,027–10,037, doi:10.1029/JA094iA08p10027.
Guicking, L., K.-H. Glassmeier, H.-U. Auster, Y. Narita, and G. Kleindienst (2012), Low-frequency magnetic field fluctuations in Earth's plasma environment observed by THEMIS, *Ann. Geophys.*, *30*, 1271–1283, doi:10.5194/angeo-30-1271-2012.
Gutynska, O., J. Šafránková, and Z. Němeček (2008), Correlation length of magnetosheath fluctuations: Cluster statistics, *Ann. Geophys.*, *26*, 2503–2513, doi:10.5194/angeo-26-2503-2008.
Gutynska, O., J. Šimůnek, J. Šafránková, Z. Němeček, and L. Přech (2012), Multipoint study of magnetosheath magnetic field fluctuations and their relation to the foreshock, *J. Geophys. Res.*, *117*, A04214, doi:10.1029/2011JA017240.
Hoppe, M. M., C. T. Russell, L. A. Frank, T. E. Eastman, and E. W. Greenstadt (1981), Upstream hydromagnetic waves and their association with backstreaming ion populations—ISEE 1 and 2 observations, *J. Geophys. Res.*, *86*, 4471–4492, doi:10.1029/JA086iA06p04471.
Hoppe, M. M., C. T. Russell, T. E. Eastman, and L. A. Frank (1982), Characteristics of the ULF waves associated with upstream ion beams, *J. Geophys. Res.*, *87*, 643–650, doi:10.1029/JA087iA02p00643.
Hwang, K.-J., M. M. Kuznetsova, F. Sahraoui, M. L. Goldstein, E. Lee, and G. K. Parks (2011), Kelvin-Helmholtz waves under southward interplanetary magnetic field, *J. Geophys. Res.*, *116*, A08210, doi:10.1029/2011JA016596.
Johnson, J. R., and C. Z. Cheng (1997), Kinetic Alfvén waves and plasma transport at the magnetopause, *Geophys. Res. Lett.*, *24*, 1423–1426, doi:10.1029/97GL01333.
Kennel, C. F., J. P. Edmiston, and T. Hada (1985), A Quarter Century of Collisionless Shock Research, in *Collisionless Shocks in the Heliosphere: Review of Current Research, Geophys. Monogr. Ser.*, vol. 35, edited by R. G. Stone and B. T. Tsurutani, pp. 1–36, AGU, Washington, D. C.
King, J. H., and N. E. Papitashvili (2005), Solar wind spatial scales in and comparisons of hourly Wind and ACE plasma and magnetic field data, *J. Geophys. Res.*, *110*, A02104, doi:10.1029/2004JA010649.
Lacombe, C., G. Belmont, D. Hubert, C. C. Harvey, A. Mangeney, C. T. Russell, J. T. Gosling, and S. A. Fuselier (1995), Density and magnetic field fluctuations observed by ISEE 1-2 in the quiet magnetosheath, *Ann. Geophys.*, *13*, 343-357, doi:10.1007/s00585-995-0343-1.
Lavraud, B., et al. (2013), Asymmetry of magnetosheath flows and magnetopause shape during low Alfvén Mach number solar wind, *J. Geophys. Res. Space Physics*, *118*, 1089–1100, doi:10.1002/jgra.50145.
Longmore, M., S. J. Schwartz, J. Geach, B. M. A. Cooling, I. Dandouras, E. A. Lucek, and A. N. Fazakerley (2005), Dawn-dusk asymmetries and sub-Alfvénic flow in the high and low latitude magnetosheath, *Ann. Geophys.*, *23*, 3351–3364, doi:10.5194/angeo-23-3351-2005.
Lucek, E. A., M. W. Dunlop, T. S. Horbury, A. Balogh, P. Brown, P. Cargill, C. Carr, K.-H. Fornaçon, E. Georgescu, and T. Oddy (2001), Cluster magnetic field observations in the magnetosheath: Four-point measurements of mirror structures, *Ann. Geophys.*, *19*, 1421–1428, doi:10.5194/angeo-19-1421-2001.
Luhmann, J. G., C. T. Russell, and R. C. Elphic (1986), Spatial distributions of magnetic field fluctuations in the dayside magnetosheath, *J. Geophys. Res.*, *91*(A2), 1711–1715, doi:10.1029/JA091iA02p01711.
Lyon, J. (1994), MHD simulations of the magnetosheath, *Adv. Space Res.*, *14*(7), 21–28, doi:10.1016/0273-1177(94)90043-4.
McFadden, J. P., C. W. Carlson, D. Larson, M. Ludlam, R. Abiad, B. Elliott, P. Turin, M. Marckwordt, and V. Angelopoulos (2008), The THEMIS ESA plasma instrument and in-flight calibration, *Space Sci. Rev.*, *141*(1-4), 277-302, doi:10.1007/s11214-008-9440-2.
Němeček, Z., J. Šafránková, G. N. Zastenker, P. Pišoft, K. I. Paularena, and J. D. Richardson (2000), Observations of the radial magnetosheath profile and a comparison with gasdynamic model predictions, *Geophys. Res. Lett.*, *27*(17), 2801–2804, doi:10.1029/2000GL000063.
Němeček, Z., J. Šafránková, G. Zastenker, P. Pišoft, and K. Jelínek (2002), Low-frequency variations of the ion flux in the magnetosheath, *Planet. Space Sci.*, *50*(5-6), 567–575, doi:10.1016/S0032-0633(02)00036-3.
Nykyri, K. (2013), Impact of MHD shock physics on magnetosheath asymmetry and Kelvin-Helmholtz instability, *J. Geophys. Res. Space Physics*, *118*, 5068–5081, doi:10.1002/jgra.50499.
Papadopoulos, K. (1985), Microinstabilities and anomalous transport, in *Collisionless Shocks in the Heliosphere: A Tutorial Review, Geophys. Monogr. Ser.*, vol. 34, edited by R. G. Stone and B. T. Tsurutani, pp. 59–90, AGU, Washington, D. C.
Paularena, K. I., J. D. Richardson, M. A. Kolpak, C. R. Jackson, and G. L. Siscoe (2001), A dawn-dusk density asymmetry in Earth's magnetosheath, *J. Geophys. Res.*, *106*, 25,377–25,394, doi:10.1029/2000JA000177.
Petrinec, S. M., T. Mukai, A. Nishida, T. Yamamoto, T. K. Nakamura, and S. Kokubun (1997), Geotail observations of magnetosheath flow near the magnetopause, using Wind as a solar wind monitor, *J. Geophys. Res.*, *102*, 26,943–26,960, doi:10.1029/97JA01637.
Russell, C., and M. Hoppe (1983), Upstream waves and particles, *Space Sci. Rev.*, *34*(2), 155–172, doi:10.1007/BF00194624.
Russell, C. T., and R. C. Elphic (1979), ISEE observations of flux transfer events at the dayside magnetopause, *Geophys. Res. Lett.*, *6*, 33–36, doi:10.1029/GL006i001p00033.

Sagdeev, R. Z. (1966), Cooperative phenomena and shock waves in collisionless plasmas, *Rev. Plasma Phys.*, *4*, 23–90.
Sagdeev, R. Z., and A. A. Galeev (1969), *Nonlinear Plasma Theory*, W. A. Benjamin, New York.
Scholer, M., and T. Terasawa (1990), Ion reflection and dissipation at quasi-parallel collisionless shocks, *Geophys. Res. Lett.*, *17*, 119–122, doi:10.1029/GL017i002p00119.
Schwartz, S. J., D. Burgess, and J. J. Moses (1996), Low-frequency waves in the Earth's magnetosheath: Present status, *Ann. Geophys.*, *14*(11), 1134–1150.
Shevyrev, N., and G. Zastenker (2005), Some features of the plasma flow in the magnetosheath behind quasi-parallel and quasi-perpendicular bow shocks, *Planet. Space Sci.*, *53*(1-3), 95–102, doi:10.1016/j.pss.2004.09.033.
Shevyrev, N., G. Zastenker, P. Eiges, and J. Richardson (2006), Low frequency waves observed by Interball-1 in foreshock and magnetosheath, *Adv. Space Res.*, *37*(8), 1516–1521, doi:10.1016/j.asr.2005.07.072.
Shevyrev, N. N., G. N. Zastenker, and J. Du (2007), Statistics of low-frequency variations in solar wind, foreshock and magnetosheath: INTERBALL-1 and CLUSTER data, *Planet. Space Sci.*, *55*, 2330–2335, doi:10.1016/j.pss.2007.05.014.
Shue, J.-H., et al. (1998), Magnetopause location under extreme solar wind conditions, *J. Geoplys. Res.*, *103*, 17,691–17,700, doi:10.1029/98JA01103.
Sibeck, D. G. (1992), Transient events in the outer magnetosphere—Boundary waves of flux transfer events?, *J. Geophys. Res.*, *97*, 4009–4026, doi:10.1029/91JA03017.
Soucek, J., and C. P. Escoubet (2011), Cluster observations of trapped ions interacting with magnetosheath mirror modes, *Ann. Geophys.*, *29*, 1049–1060, doi:10.5194/angeo-29-1049-2011.
Soucek, J., E. Lucek, and I. Dandouras (2008), Properties of magnetosheath mirror modes observed by Cluster and their response to changes in plasma parameters, *J. Geophys. Res.*, *113*, A04203, doi:10.1029/2007JA012649.
Spreiter, J. R., A. L. Summers, and A. Y. Alksne (1966), Hydromagnetic flow around the magnetosphere, *Planet. Space Sci.*, *14*, 223–250, doi:10.1016/0032-0633(66)90124-3.
Verigin, M. I., et al. (2001), Analysis of the 3-D shape of the terrestrial bow shock by INTERBALL/MAGION 4 observations, *Adv. Space Res.*, *28*, 857–862, doi:10.1016/S0273-1177(01)00502-6.
Verigin, M. I., M. Tátrallyay, G. Erdös, and G. A. Kotova (2006), Magnetosheath interplanetary medium reference frame: Application for a statistical study of mirror type waves in the terrestrial plasma environment, *Adv. Space Res.*, *37*, 515–521, doi:10.1016/j.asr.2005.03.042.
Walsh, B. M., D. G. Sibeck, Y. Wang, and D. H. Fairfield (2012), Dawn-dusk asymmetries in the Earth's magnetosheath, *J. Geophys. Res.*, *117*, A12211, doi:10.1029/2012JA018240.
Wilson, L. B., et al. (2013), Electromagnetic waves and electron anisotropies downstream of supercritical interplanetary shocks, *J. Geophys. Res. Space Physics*, *118*, 5–16, doi:10.1029/2012JA018167.
Wing, S., J. R. Johnson, P. T. Newell, and C.-I. Meng (2005), Dawn-dusk asymmetries, ion spectra, and sources in the northward interplanetary magnetic field plasma sheet, *J. Geophys. Res.*, *110*, A08205, doi:10.1029/2005JA011086.
Yao, Y., C. C. Chaston, K.-H. Glassmeier, and V. Angelopoulos (2011), Electromagnetic waves on ion gyro-radii scales across the magnetopause, *Geophys. Res. Lett.*, *38*, L09102, doi:10.1029/2011GL047328.
Zastenker, G. N., M. N. Nozdrachev, Z. Němeček, J. Šafránková, K. I. Paularena, J. D. Richardson, R. P. Lepping, and T. Mukai (2002), Multispacecraft measurements of plasma and magnetic field variations in the magnetosheath: Comparison with Spreiter models and motion of the structures, *Planet. Space Sci.*, *50*(5-6), 601–612, doi:10.1016/S0032-0633(02)00039-9.